Signatures of distinct impurity configurations in atomic-resolution valence electron-energy-loss spectroscopy: Application to graphene

Myron D. Kapetanakis, Mark P. Oxley, Wu Zhou, Stephen J. Pennycook, Juan-Carlos Idrobo, and Sokrates T. Pantelides

Phys. Rev. B **94**, 155449 — Published 31 October 2016

DOI: 10.1103/PhysRevB.94.155449

Signatures of distinct impurity configurations in atomic-resolution valence-electron-energy-loss spectroscopy – application to graphene

Myron D. Kapetanakis[1,2,*], Mark P. Oxley[2,1,*], Wu Zhou[2,**], Stephen J. Pennycook[3], Juan-Carlos Idrobo[4], and Sokrates T. Pantelides[1,2]

[1.] Department of Physics and Astronomy, Vanderbilt University, Nashville, TN, USA.
[2.] Material Science and Technology Division, Oak Ridge National Laboratory, Oak Ridge, TN, USA.

[3.] Department of Materials Science and Engineering, National University of Singapore, Singapore 117575

[4.] Center for Nanophase Materials Sciences Division, Oak Ridge National Laboratory, Oak Ridge, TN, USA.

[*]myron.kapetanakis@Vanderbilt.Edu; oxleymp@ornl.gov
[**]Current address: School of Physical Sciences, CAS Key Laboratory of Vacuum Physics, University of Chinese Academy of Sciences, Beijing 100049, China.

The detection and identification of impurities and other point defects in materials is a challenging task. Signatures for point defects are typically obtained using spectroscopies without spatial resolution. Here we demonstrate the power of valence-electron energy-loss spectroscopy (VEELS) in an aberration-corrected scanning transmission electron microscope (STEM) to provide energy- and atomically-resolved maps of electronic excitations of individual impurities **which, combined with theoretical simulations, yield** unique signatures of distinct bonding configurations of impurities. We report VEELS maps for isolated Si impurities in graphene, which are known to exist in two distinct configurations. We also report simulations of the maps, based on density functional theory and dynamical scattering theory, which agree with and provide direct interpretation of observed features. We show that **theoretical** VEELS maps exhibit distinct and unambiguous signatures for the threefold- and fourfold-coordinated configurations of Si impurities in different energy-loss windows, corresponding to impurity-induced bound states, resonances, and antiresonances. With the advent of new monochromators and detectors with high energy resolution and low signal-to-noise ratio the present work ushers an atomically-resolved STEM-based spectroscopy of individual impurities as an alternative to conventional spectroscopies for probing impurities and defects.

I. INTRODUCTION

Impurities and defects are the primary agents for functionalizing materials[1-3]. For example, dopant impurities in semiconductors enable the formation of *pn* junctions, which are the building blocks of electronic devices. Furthermore defect/impurity engineering in materials constitutes a driving force for the realization of devices, e.g., for solar panels and light-emitting-diode applications[4-6]. At the same time, impurities and defects limit performance by degrading carrier mobilities or by serving as recombination centers and can mediate device degradation[3,7-9]. Impurities and defects have the same role in two-dimensional (2D) materials[10-12]. The detection and identification of undesirable impurities and process-induced defects is, therefore, necessary to guide device design.

In bulk materials, the majority of existing methods probe defects by inducing emission or capture of electrons or holes at the defects' localized states by optical, thermal, or electrical means or by detecting unpaired spins[2]. Such methods lack spatial resolution, provide very limited defect-specific information (typically only energy levels), and require fairly large concentrations. The identification of defects and impurities on surfaces or 2D materials can be achieved by atomic force microscopy[13] (AFM) or scanning tunneling microscopy (STM) and spectroscopy[14-16] (STS). In both 2D and 3D materials, atomic-resolution scanning-transmission-electron-microscopy (STEM) images provide structural information that can aid identification if the atomic number Z of impurities is larger than those of host atoms[17] (the signal intensity is roughly proportional to Z^2). Simultaneously collected spectra in core-loss electron-energy-loss spectroscopy (EELS) provide chemical information as each element has characteristic "edges" and electron-loss near-edge structure (ELNES)[18-20]. However, identification and detailed characterization of defects in 3D materials still remains a challenging task.

In this paper we demonstrate that valence electron-energy-loss spectroscopy (VEELS) in an aberration-corrected STEM can be a powerful complementary tool for the identification of different atomic configurations of defects. VEELS spectra are many orders of magnitude stronger than core-loss spectra[21], producing high signal-to-noise ratios with shorter irradiation times, which result in limited structural damage or chemical rearrangements that are often observed in core-loss EELS[22]. There was a common belief that VEELS have inherently limited spatial resolution, making atomic resolution all but impossible[23-26]. In recent work, however, we demonstrated that, in a perfect region of monolayer graphene, integration of a VEELS spectrum over selected energy windows as a function of probe position yields detailed 2D maps with atomic-scale contrast[27]. Corresponding simulations carried out by combining density functional theory (DFT) calculations and dynamical scattering theory enable the identification of the type of electronic transitions that are responsible for the observed features. Here we demonstrate that aberration-corrected-STEM VEELS maps with sufficient spatial resolution can be obtained for individual Si impurities in graphene, which are known to exist in two

distinct configurations: threefold, replacing a single C atom, and fourfold-coordinated, replacing two C atoms (the identification was made by Z-contrast images and core-loss EELS[18,20]). **It is well established that the existence of impurities in graphene induces a strongly localized signal within the energy range of interest[28,29].** We use a combination of DFT and dynamical scattering theory to simulate these maps and find them to agree with the corresponding experimental maps. We demonstrate that, in a series of energy windows, the VEELS maps exhibit features that are unambiguous signatures of the threefold- and fourfold-coordinated configurations of Si impurities. The features originate from transitions associated with bound states, resonances, and antiresonances induced by individual impurities, as opposed to the average signals obtained by photon-based spectroscopies, which are usually very weak unless a large concentration of impurities is present. The method presented here promises to provide an atomically-resolved probe of electronic excitations within the optical-energy range, which do not obey the optical selection rules since they require a nonzero amount of momentum transferred to the valence electron. The unprecedented wealth of information that can be derived from excitations up to 100 eV, demonstrated here for impurities in a 2D material, promises enormous power to probe *individual* impurities and defects in 3D materials as new generations of monochromators offer new meV-scale energy resolution[30,31] and new generations of solid-state detectors can offer very low signal-to-noise ratios. Application to 3D materials may of course encounter additional difficulties that will need to be overcome.

II. STEM/VEELS experimental data of silicon impurities in graphene.

The STEM-VEELS experiments were performed with a Nion UltraSTEM, equipped with a cold field emission electron source and a corrector of third and fifth order aberrations, operating at 60 kV accelerating voltage. After aberration correction, this microscope is capable of providing 1.065 Å information transfer limit in Z-contrast imaging, with a probe current of ~110 pA. EEL spectra were collected using a Gatan Enfina spectrometer, with an energy resolution of 0.5 eV for 0.1 eV/channel energy dispersion. The convergence semi-angle for the incident probe was ~30 mrad, with an EELS collection semi-angle of ~48 mrad. In order to increase the signal-to-noise ratio and avoid non-locality effects, the majority of scattered electrons are collected. For the results shown in this manuscript, EEL spectrum images were collected from 0.5 to 134.5 eV energy-loss range with 0.1 eV/channel dispersion, 0.05 s/pixel dwell time, an electron dose of $5x10^8$ electrons per Si atom, and 0.257 Å pixel size. **Within such experimental conditions we can achieve a higher signal-to-noise ratio for the higher energy losses, where the focus of the present paper is on.** Annular-dark-field (ADF) images were collected from ~86 to 200 mrad half-angle range.

Fig. 1 shows STEM-VEEL spectrum imaging of silicon impurities in a graphene monolayer. The inset of Fig. 1 shows a STEM ADF image of a graphene monolayer which allows us to identify an isolated fourfold-coordinated impurity. The comparison of the signal intensity at the position of the impurity with the intensity at the carbon

positions reveals that it comprises a silicon atom. The ADF image was simultaneously acquired with a valence electron energy loss (VEEL) spectrum image, i.e., a VEEL spectrum (VEELS) is collected and stored at every pixel in the image. Fig. 1a shows the averaged VEELS, with the so-called $\pi+\sigma$ peak clearly seen at 15 eV. **The π peak, which is located at 4.5 eV for pristine graphene (see, for instance, Refs [27,28]) was masked due to the limited energy resolution and tip noise fluctuations in this particular experiment.**

The effect of the impurities can be demonstrated by spatially-resolved VEELS maps obtained by plotting the VEELS intensity integrated in different energy-loss windows from the raw data, without any background subtraction or filtering, as a function of probe position. Such windows must be fairly large in order to minimize the statistical noise that exists in the data and produce maps with high signal-to-noise ratios. The VEELS maps for the energy windows, 11-22 eV and 22-44 eV, highlighted in Fig. 1a, are shown in Figs 1b and 1c respectively. **By directly comparing with the ADF image, shown in the inset of Fig. 1a, we observe that the carbon atoms cannot be resolved in the lower-energy map (Fig. 1b). However, atomic resolution is present in the higher-energy VEELS map (Fig. 1c) where the carbon atoms of the graphene structure are clearly resolved. Since the two windows have comparable contrast levels (Fig. 1d), this shows the signal does not arise from preservation of elastic scattering but reflects true atomic resolution variation of the EEL scattering probability.** The silicon impurity exhibits higher contrast in the VEELS map from the 11-22-eV energy-loss window (Fig. 1c). The full width at half maximum (FWHM) for the bright spot within the 11-22 eV range is about 4 Å while the intensity at the impurity position is about 4% larger than the background, as shown by the red circles in Fig. 1d. For the higher energies (22-44 eV), on the other hand, we observe that the impurity becomes a dark hole with respect to the surrounding area (Fig. 1d) since the corresponding intensity is significantly reduced. This reverse-contrast image has a similar localization to that of the image in Fig. 1c. We also performed STEM-VEEL spectrum imaging with different EELS collection semi-angles (15 mrad, 35 mrad), different energy dispersions (0.05 eV/channel, 0.3 eV/channel) and different energy-loss collection onsets. The obtained atomically-resolved VEEL spectrum images were consistent with those shown in Fig. 1.

In order to ensure that the observed features arise from relatively isolated impurities we collected larger-scale images which we show in Fig. 2. In this way we demonstrate that the silicon impurity is at least 3 nm away, and thus well isolated, from any contamination or other defects. The green box in Fig. 2 indicates the area where the STEM/VEELS signal of Fig. 1 was acquired. The collected VEELS data for the fourfold silicon impurity are not, therefore, affected by proximity to any other defect or contamination.

We were also able to collect VEELS data for a threefold-coordinated silicon impurity, which are shown in Fig. 3. Fig. 3a shows a low magnification ADF image of the graphene monolayer displaying a threefold coordinated silicon impurity and a number of contaminants nearby. The ADF image that corresponds to the green box around the silicon impurity in Fig. 3a is shown in Fig. 3b. By integrating the spectroscopic data over the 11—22 eV and 22—44 eV energy windows we construct the VEELS maps of Fig. 3c and Fig. 3d correspondingly. The circles in Figs 3b--d indicate the position of the silicon atom as determined by the ADF image Fig. 3b. We observe that the 3-fold Si defect is fairly close to other defects, as one can see from the continuously decaying background

in the VEELS map of 11-22 eV. However, the enhancement for 11-22 eV and dark contrast for 22-44eV can still be observed at the Si site. Fig. 3 shows, therefore, that the spatial resolution of the measured maps is limited due to high level of noise and the contamination of the nearby environment.

III. THEORY

A. The localization of the valence electronic excitations.

As first demonstrated in ref [27], VEELS signals can produce spatially localized maps even in the absence of impurities or defects. In the case of a single impurity atom, such as discussed above, one might intuitively expect an enhancement of the VEELS signal localized about the impurity and consider this to be due to the excitation of impurity bound states. The amount of localization of such states can be qualitatively assessed by projecting an electronic state at a spherical harmonic centered at the crystal position of interest $\langle \Psi_{nk} | lm \rangle$ and produce the so-called partial Density of States (PDOS). The main effect of an impurity on the band structure of a material is the introduction of bound states, resonances and antiresonaces that are strongly localized in the vicinity of the impurity[32]. In the same spirit with the definition of PDOS we introduce the *partial Joint Density of States* (PJDOS),

$$\rho_{lml'm'}(E) = \sum_{i,j} \langle i | lm \rangle \langle l'm' | f \rangle \delta(E - E_i + E_f) \quad (1)$$

which describes the density of possible electronic excitations with respect to the energy-loss E at the vicinity of a selected atom. The PJDOS, a useful quantity for the purposes of this paper, provides a qualitative description of the energy-dependence and the atomic character of the underlying electronic excitations. The *lm*-decomposion of the initial and the final state allows us to calculate the PJDOS of any lm→l'm' excitation, such as $p_z \rightarrow p_z$ or $sp^2 \rightarrow sp^2$, which are convenient for the hexagonal-symmetry structures used here which do not obey the optical selection rules. We remind the reader that EELS includes excitations with any momentum transfer so that the usual selection rules for optical excitations do not apply. Within this scheme we make the distinction between excitations that are localized around the silicon impurity and the ones that occur around the carbon atoms of the host lattice. Note that the PJDOS only provides a qualitative description of the available electronic excitations and their population as a function of the energy loss E. To determine the probability of any particular excitation to occur one has to consider the corresponding transition matrix element and calculate the actual EEL spectrum as described below.

B. Construction of the VEELS maps.

The transition induced by the fast electron between different electronic states within a crystal is mediated by the Coulomb interaction and is expressed by the transition matrix element

$$H_{if}\left(\mathbf{q}_{\perp}\right) \propto \left. \frac{\left\langle \Psi_f\left(\mathbf{r}\right) \middle| e^{-2\pi i \mathbf{q}\cdot\mathbf{r}} \middle| \Psi_i\left(\mathbf{r}\right) \right\rangle}{\mathbf{q}^2} \right|_{q_z} . \quad (2)$$

Here $\left|\Psi_i(\mathbf{r})\right\rangle$ and $\left|\Psi_f(\mathbf{r})\right\rangle$ are the electronic wave functions, calculated within the DFT method, for the initial and final electronic state, respectively, and $\boldsymbol{q}$ is the momentum transfer to the crystal. The component q_z along the beam (z) direction is determined by the energy-loss $E_{Loss} = E_f - E_i$ and the incident energy E_0 of the electron's probe by the formula $q_z \simeq k_0 E_{Loss}/2E_0$. The relative size of the probe forming and detector angles used in the STEM/VEELS experiment, 30 and 48 mrad. respectively, are such that the majority of the scattered electrons are collected. The latter allows us to work within the local approximation[33-35] and calculate the inelastic scattering potential for a particular energy loss E_{LOSS}=E_f-E_i by

$$V_{i,f}\left(\mathbf{R}, E_{LOSS}\right) \propto \left|H_{i,f}\left(\mathbf{R}\right)\right|^2 \delta\left(E_{LOSS} - E_i + E_f\right). \quad (3)$$

For a 2D system, we may neglect channeling effects of the fast electron and write the image formed by the underlying electronic excitations

$$I_{n0}\left(\mathbf{R}_0, E_{LOSS}\right) \propto \left|P\left(\mathbf{R}_0, \mathbf{R}\right)\right|^2 \otimes V_{i,f}\left(\mathbf{R}, E_{LOSS}\right), \quad (4)$$

as a convolution with the probe intensity, considered constant in the perpendicular direction z over the effective range of the projected potential[27,35]. By integrating Eq. (4) over the desired energy-loss range we can now calculate the intensity of a VEELS map as a function of the probe intensity and directly compare with the experimental data. Furthermore, the average VEEL spectrum as a function of E_{LOSS} is obtained by averaging the VEELS intensity with respect to the probe position. To demonstrate the effect of a particular atom, for instance an impurity, we can calculate an average spectrum by averaging over a particular area around the atom of interest instead of the whole supercell.

IV. RESULTS AND DISCUSSION

A. Calculation of VEELS maps and comparison with the data.

Using Eqs. (3)-(4) we simulated the effect of both a fourfold- and a threefold-coordinated silicon impurity on the STEM/VEELS maps of monolayer graphene. The initial and final electronic wavefunctions are calculated within Density Functional Theory (DFT). We carry out the DFT calculations by using the Vienna ab initio Simulations Package (VASP)[36-39]. We also work within the Generalised Gradient Approximation (GGA) while we take into account the projector-augmented wave (PAW) corrections[36,39], which are essential for the proper treatment of the low momentum transfer limit (dipole approximation). To simulate an isolated impurity an expanded $5\times5\times1$ graphene supercell was used. In order to correctly model the vacuum on either side of a graphene sheet we increased the size to about 30 Å along the perpendicular

direction**.** The Brillouin zone was sampled by using a $2\times2\times1$ k-point mesh, which is enough for obtaining a relaxed density of states.

The spatially-resolved maps are calculated by integrating the intensity given by Eq. (4) over particular energy windows. We first integrate over the same energy windows that we used for constructing the experimental VEELS maps of Fig. 1 and directly compare with the data shown in Fig. 1, while simulated maps in smaller energy windows are shown in Fig. 5. Fig. 4a shows the calculated VEELS maps for the fourfold-coordinated Si, which are in good agreement with the experimental data. Both the intensity enhancement in the low-energy window as well as the diminishment in the higher-energy window at the silicon position are reproduced. A line profile analysis of the map, Fig. 4a, shows a FWHM of about 2 Å and an intensity enhancement of about 10% compared with the carbon positions.

The calculated VEELS maps for the threefold-coordinated impurity in the same energy windows are shown in Figure 4b. Although the intensity at the silicon atom is enhanced in the low-energy window, similar to the fourfold-coordinated case, for the higher energies, the intensity remains strong and is clearly higher than at the first neighboring carbon atom, as shown in the line profile Figure 4c. It is clear, therefore, that the VEELS signal within the low-energy energy window does not distinguish between the bonding configurations. In contrast, the VEELS signal in the 22-45-eV window provides characteristic signatures for the two configurations. We conclude that VEELS signals, at least in some energy windows, depend on the character of the chemical bonding between an impurity and host. We will show shortly that maps obtained by integrating over smaller energy windows provide an array of distinct signatures for the two Si configurations, but such maps are currently only possibly using simulated VEELS because of excessive noise in the experimental VEELS.

B. VEELS spectra modulation due to impurities.

In Figs 5a and 5g, we compare the calculated VEEL spectra for each of the two Si configurations with the spectrum for pristine graphene. All spectra in Figs 5a and 5g were obtained by integrating Eq. (4) over an area about 2 $Å^2$ **(**8×8 pixels**)** around the silicon impurities or a carbon atom for the pristine-graphene VEELS**.** We see that both silicon impurities enhance strongly the VEEL intensity around the edge of the π+σ peak (10—16 eV), while their effect is weaker around the positions of the π and π+σ peaks as well as for higher energy losses (>20 eV).

To identify the origin of the impurity-induced changes in the VEEL spectra we calculated the PJDOS using Eq. (1), for the two silicon configurations and compare it with the PJDOS for pristine graphene in Figs 5b and 5h. In Figs 5b and 5h we show the *lm*-decomposed PJDOS projected at the silicon position for each of the two Si configurations. The curves in Figs 5b and h show the density of excitations in graphene from states with sp^2 (solid line) or p_z (dashed line) atomic character. We see that the population of excitations localized at the atomic positions of graphene is high, around 30 eV, for sp^2 character, and low, around 5 eV, for p_z character. We see that, around the silicon impurities, the excitations with an sp^2 character *redshift* to lower energies as compared to the pristine graphene. The qualitative difference between the two impurity configurations appears at the higher energy regime (>20 eV) where a significant density

of sp^2 excitations for the three-fold coordinated impurity exists, whereas the corresponding density for the four-fold coordinated impurity is low. Additionally, the formation of a sp^2d hybridization --since the d_{xy} and $d_{x^2-y^2}$ states (denoted as d_{in} in Fig. 5b) contribute to the chemical bond of the fourfold-coordinated configuration in order to accommodate the symmetry of the bonding-- it opens an additional channel for excitations (colored green in Fig. 5a) with a d_{in} character at about the 30 eV energy window. Such excitations are negligible at the case of the threefold-coordinated impurity (see Fig. 5h) due to the absence of occupied d-states (we have the formation of a sp^3-like hybridization).[28]

By comparing the spectra in Figs 5a and 5g with the PJDOS in Figs 5b and 5h correspondingly, we can directly associate the high population of sp^2 excitations, around the vicinity of the silicon impurity, with the strong enhancement of the VEELS spectra that takes place in the 10-15 eV window. No further information, however, can be obtained from solely considering the spectra.

C. Spatially-resolved signatures of impurities in the VEELS maps.

Within the framework of the method presented here we are able to calculate spatially resolved maps within narrower energy windows than those used in Fig. 1. The experimental measurement of such maps is a challenging task due to the level of noise, which requires integrating over wide energy windows. **Using our current microscope, it has not been possible to obtain maps with adequate signal-to-noise ratio when integrating over 5-eV windows. We therefore use theoretical maps to demonstrate the power of the method in anticipation of improved instrumentation.** We calculated the four VEELS maps shown in Figs 5c-f within the energy windows 9-14 eV (Fig. 5c), 16-21 eV (Fig. 5d), 22-27 eV (Fig. 5e) and 28-33 eV (Fig. 5f). These maps are characteristic signatures of the fourfold-coordinated Si impurity and reveal the rich effects of the silicon impurity on the VEELS in a much more vivid way than the line spectra of Fig. 3a, especially in the higher-energy windows. Within the 9-14 eV window the intensity at the impurity is strongly enhanced. The enhancement is directly associated with the high population of sp^2 excitations in the vicinity of the impurity compared with those in the vicinity of a carbon atom (Fig. 5b). For slightly higher energies, i.e. 16-21 eV, the population of the excitations in the vicinity of the silicon impurity is still large. However these excitations coexist with a significant population of excitations that are localized around the host carbon atoms, resulting in the map in Fig. 5d, where strong intensity exists through the whole supercell. Eventually, the graphene-like excitations become dominant in the 22-27 eV window and the silicon impurity appears as a dark spot in the corresponding map (Fig. 5e). Finally, the intensity at the silicon position increases again in the higher-energy window, 28-33 eV, as a weak population of d_{in} excitations arises.

To compare with the four-fold coordinated silicon impurity, and demonstrate the qualitative differences between the two bonding configurations, we consider the threefold-coordinated silicon impurity and calculate the maps in Figs 5i-l within the same energy windows as in Figs 5e-f. The corresponding VEELS maps for a threefold-coordinated Si impurity are significantly different and again represent unique signatures. For the lower energy windows, 9-14 eV (i) and 16-21 eV (j), the VEELS maps display a

strong enhancement around the impurity that is similar to the Si-C_4 result. The enhancement is associated with the redshift of the sp^2 excitations, which is present in both configurations. The existence of a non-negligible density of excitations at the higher energy losses, in contrast to the four-fold coordinated impurity, affects the character of the obtained VEELS maps in the higher energy windows, 22-27 eV (k) and 28-33 eV (l). The map in the 22-27 eV window (Fig. 5k) shows a significant intensity around the threefold-coordinated impurity, which becomes very strong in the higher-energy window (Fig. 5l). Both maps (Figs 5k-l) reflect the existence of the high density of sp^2 excitations for the higher energy windows in the vicinity of the threefold-coordinated configuration, which is suppressed to lower energies due to the sp^2d bonding for the four-fold configurations. The features of the VEELS maps at the higher energy loss regime, therefore, reflect the different chemical bonding, while the existence of a structural non-periodicity has a strong effect on the maps for the intermediate energies.

D. Average VEEL spectra.

Though the magnitude of the deviations from the pristine-graphene spectrum depend on the size of the averaging region, it is clear that the impurity modifies the local VEEL spectrum over the entire energy range. As the size of the integration area increases, the effect of the silicon impurities on the VEEL spectra weakens, and eventually becomes minimal for the average spectrum. Figs 6a,b and c show the calculated VEEL spectra for pristine graphene, the system with the threefold- and the fourfold-coordinated (c) silicon impurity correspondingly for increasing integration area. The spectrum for pristine graphene is independent of the integration area since all carbon atoms are equivalent. The spectra for the systems with the Si impurities mostly differ from the pristine graphene spectrum most at the edge of the $\pi+\sigma$ peak (10—16 eV). The deviations decrease while the integration area increases and become minimum for the average spectra obtained by integration over the whole supercell (about 66 $Å^2$). The calculated average spectrum shown in Fig. 6 is in excellent agreement with the experimental average spectrum in Fig. 1b, given the uncertainties in exchange-correlation functionals that tend to yield empty states at lower energies compared to experimental values. Such discrepancies between experimental data and simulations can be alleviated by adopting a DFT/hybrid scheme of calculating the electronic structure[40,41] as well as taking into account excitonic effects, which affect the low loss spectrum of 2D materials[42].

E. Characteristic VEELS maps formed by resonant or antiresonant states.

In a semiconductor with a nonzero energy gap, impurities and point defects such as vacancies introduce localized states in the gap but also resonances (local enhancements of the density of states) and antiresonances (local depletions of the density of states)[32]. In graphene, because of the absence of an energy gap, a Si impurity introduces only resonances and antiresonances, which can be illustrated by examining the PJDOS as discussed in Fig. 5. Alternatively, resonances and antiresonances can be illustrated by considering the spatial distribution of the electron density of particular electronic states, as shown in Figures 7a (resonance – highly localized around the impurity atom) and 7c (antiresonance – virtually no amplitude around the impurity atom). Note that the state in

Fig. 7a displays a 3*d*-character around the impurity, while a residual intensity is also visible through the neighboring carbon atoms. The electronic excitation between the two resonant states – with an energy loss E_{LOSS}=30.7 eV -- form the VEELS map of Figure 7e that shows non-vanishing intensity only around the position of the impurity.

V. CONCLUSIONS

We presented a combined experimental and theoretical method that provides characteristic signatures of *individual* impurities and defects. We demonstrated the method in the case of two configurations of Si impurities in monolayer graphene for which experimental data with sufficient spatial resolution are possible with currently available instrumentation. As new instrumentation becomes available with better energy resolution and better signal-to-noise ratio, the method should have wide applicability in both 2D and 3D materials.

The method is based on probe-position-dependent VEEL spectra that are simultaneously collected with ADF images. By integrating these spectra over chosen energy windows, one constructs VEELS maps. In the case of pristine graphene, the maps reveal the underlying host lattice. In the presence of an impurity, however, the maps reveal features that arise from impurity-induced localized states (bound states, if any, resonances and antiresonances) and can serve as signatures of the impurity and its local bonding configuration. Multiple signatures exist in different energy windows in excitations that range from very low energies up to 100 eV. Given that aberration-corrected STEMs equipped with high-energy-resolution monochromators can already detect phonon excitations[30,31], the prospects of the present method to identify individual impurities in a clear and unambiguous way are very high. Finally, the future application of the method to magnetic systems will allow us to probe magnetic signals from individual impurities and open the possibility for detection of electron-loss-magnetic-chiral-dichroism[43,44] (EMCD) in the low-loss regime.

ACKNOWLEDGEMENTS

This research was supported by DOE Grant No. DE-FG02-09ER46554 (MDK, MPO, STP), by the U.S. Department of Energy Office of Science, Basic Energy Sciences, Materials Sciences and Engineering Division (MPO, WZ), the Center for Nanophase Materials Sciences (CNMS), which is sponsored at ORNL by the Scientific User Facilities Division, Office of Basic Energy Sciences, U.S. DOE (JCI). Numerical calculations were performed at the National Energy Research Scientific Computing Center (NERSC), which is supported by the Office of Science of the U.S. Department of Energy under Contract No. DE-AC02-05CH11231.

AUTHOR CONTRIBUTIONS

W. Z. and J.C.I. carried out the experiments. M. D. K., M. P. O. and S. T. P. performed the theoretical calculations. The manuscript was written through contributions of all authors. All authors have given approval to the final version of the manuscript.

COMPETING FINANCIAL INTEREST

The authors declare no competing financial interest.

REFERENCES

[1] P. M. Koenraad, M. E. Flatte, Single dopants in semiconductors, Nature Mater. **10**, 91-100 (2011).

[2] S. T. Pantelides, *Deep centers in semiconductors* (Gordon and Breach, Switzerland, 1992).

[3] Hans J. Queisser, E. E. Haller, Defects in Semiconductors:
Some Fatal, Some Vital, Science **281**, 945 (1998).

[4] T. Buonassisi, A. A. Istratov, M. A. Marcus, B. Lai, Z. Cai, S. M. Heald, E. R. Weber, Engineering metal-impurity nanodefects for low-cost solar cells, Nat Mater **4**, 676-679 (2005).

[5] T. Andrew Taton, D. J. Norris, Defective promise in photonics, Nature **416**, 685 (2002).

[6] Xiaobo Chen, Lei Liu, Peter Y. Yu, S. S. Mao, Increasing Solar Absorption for Photocatalysis with Black Hydrogenated Titanium Dioxide Nanocrystals, Science **331**, 746 (2011).

[7] S. F. Chichibu, A. Uedono, T. Onuma, B. A. Haskell, A. Chakraborty, T. Koyama, P. T. Fini, S. Keller, S. P. Denbaars, J. S. Speck, U. K. Mishra, S. Nakamura, S. Yamaguchi, S. Kamiyama, H. Amano, I. Akasaki, J. Han, T. Sota, Origin of defect-insensitive emission probability in In-containing (Al,In,Ga)N alloy semiconductors, Nat Mater **5**, 810-816 (2006).

[8] S. T. Pantelides, Y. Puzyrev, X. Shen, T. Roy, S. DasGupta, B. R. Tuttle, D. M. Fleetwood,R. D. Schrimpf, Reliability of III–V devices – The defects that cause the trouble, Microelectronic Engineering **90**, 3-8 (2012).

[9] S. T. Pantelides, L. Tsetseris, M. J. Beck, S. N. Rashkeev, G. Hadjisavvas, I. G. Batyrev, B. R. Tuttle, A. G. Marinopoulos, X. J. Zhou, D. M. Fleetwood,R. D. Schrimpf, Performance, reliability, radiation effects, and aging issues in microelectronics – From atomic-scale physics to engineering-level modeling, Solid-State Electronics **54**, 841-848 (2010).

[10] K. Kim, J.-Y. Choi, T. Kim, S.-H. Cho,H.-J. Chung, A role for graphene in silicon-based semiconductor devices, Nature **479**, 338-344 (2011).

[11] L. Museur, A. Kanaev, Near band-gap photoluminescence properties of hexagonal boron nitride, Journal of Applied Physics **103**, 103520 (2008).

[12] S. Tongay, J. Suh, C. Ataca, W. Fan, A. Luce, J. S. Kang, J. Liu, C. Ko, R. Raghunathanan, J. Zhou, F. Ogletree, J. Li, J. C. Grossman,J. Wu, Defects activated photoluminescence in two-dimensional semiconductors: interplay between bound, charged, and free excitons, Sci Rep **3**, 2657 (2013).

[13] Y. Sugimoto, P. Pou, M. Abe, P. Jelinek, R. Perez, S. Morita,O. Custance, Chemical identification of individual surface atoms by atomic force microscopy, Nature **446**, 64-67 (2007).

[14] R. H. Liuyan Zhao, Kwang Taeg Rim, Theanne Schiros, Keun Soo Kim, Hui Zhou, Christopher Gutiérrez, S. P. Chockalingam, Carlos J. Arguello, Lucia Pálová,

Dennis Nordlund, Mark S. Hybertsen, David R. Reichman, Tony F. Heinz, Philip Kim, Aron Pinczuk, George W. Flynn, Abhay N. Pasupathy, Visualizing Individual Nitrogen Dopants in Monolayer Graphene, Science **333**, 999 (2011).
[15] K. Teichmann, M. Wenderoth, S. Loth, R. G. Ulbrich, J. K. Garleff, A. P. Wijnheijmer,P. M. Koenraad, Controlled Charge Switching on a Single Donor with a Scanning Tunneling Microscope, Physical Review Letters **101**, 076103 (2008).
[16] D. Wong, J. Velasco Jr, L. Ju, J. Lee, S. Kahn, H.-Z. Tsai, C. Germany, T. Taniguchi, K. Watanabe, A. Zettl, F. Wang,M. F. Crommie, Characterization and manipulation of individual defects in insulating hexagonal boron nitride using scanning tunnelling microscopy, Nat Nano **10**, 949-953 (2015).
[17] M. Varela, A. R. Lupini, K. v. Benthem, A. Y. Borisevich, M. F. Chisholm, N. Shibata, E. Abe, S. J. Pennycook, Materials Characterization In The Aberration-Corrected Scanning Transmission Electron Microscope, Annual Review of Materials Research **35**, 539-569 (2005).
[18] Q. M. Ramasse, C. R. Seabourne, D.-M. Kepaptsoglou, R. Zan, U. Bangert,A. J. Scott, Probing the Bonding and Electronic Structure of Single Atom Dopants in Graphene with Electron Energy Loss Spectroscopy, Nano Letters **13**, 4989-4995 (2013).
[19] M. Varela, S. D. Findlay, A. R. Lupini, H. M. Christen, A. Y. Borisevich, N. Dellby, O. L. Krivanek, P. D. Nellist, M. P. Oxley, L. J. Allen,S. J. Pennycook, Spectroscopic imaging of single atoms within a bulk solid, Phys Rev Lett **92**, 095502 (2004).
[20] W. Zhou, M. D. Kapetanakis, M. P. Prange, S. T. Pantelides, S. J. Pennycook,J.-C. Idrobo, Direct Determination of the Chemical Bonding of Individual Impurities in Graphene, Physical Review Letters **109**, 206803 (2012).
[21] F. J. García de Abajo, Optical excitations in electron microscopy, Reviews of Modern Physics **82**, 209-275 (2010).
[22] T. Susi, J. Kotakoski, D. Kepaptsoglou, C. Mangler, T. C. Lovejoy, O. L. Krivanek, R. Zan, U. Bangert, P. Ayala, J. C. Meyer,Q. Ramasse, Silicon-carbon bond inversions driven by 60-keV electrons in graphene, Phys Rev Lett **113**, 115501 (2014).
[23] R. F. Egerton, Limits to the spatial, energy and momentum resolution of electron energy-loss spectroscopy, Ultramicroscopy **107**, 575-586 (2007).
[24] R. Erni, N. D. Browning, Valence electron energy-loss spectroscopy in monochromated scanning transmission electron microscopy, Ultramicroscopy **104**, 176-192 (2005).
[25] K. Van Benthem, R. French, W. Sigle, C. Elsässer,a. M. Rühle, Valence electron energy loss study of Fe-doped $SrTiO_3$ and a $\sum 13$ boundary: electronic structure and dispersion forces, Ultramicroscopy **86** (2001).
[26] D. A. Muller, J. Silcox, Delocalization in inelastic scattering, Ultramicroscopy **59** (1995).
[27] M. D. Kapetanakis, W. Zhou, M. P. Oxley, J. Lee, M. P. Prange, S. J. Pennycook, J. C. Idrobo, S. T. Pantelides, Low-loss electron energy loss spectroscopy: An atomic-resolution complement to optical spectroscopies and application to graphene, Physical Review B **92**, 125147 (2015).
[28] W. Zhou, J. Lee, J. Nanda, S. T. Pantelides, S. J. Pennycook, J.-C. Idrobo, Atomically localized plasmon enhancement in monolayer graphene, Nat Nano **7**, 161-165 (2012).

[29] R. A. Muniz, H. P. Dahal, A. V. Balatsky,S. Haas, Impurity-assisted nanoscale localization of plasmonic excitations in graphene, Physical Review B **82**, 081411R (2010).
[30] R. Egoavil, N. Gauquelin, G. T. Martinez, S. Van Aert, G. Van Tendeloo,J. Verbeeck, Atomic resolution mapping of phonon excitations in STEM-EELS experiments, Ultramicroscopy **147**, 1-7 (2014).
[31] O. L. Krivanek, T. C. Lovejoy, N. Dellby, T. Aoki, R. W. Carpenter, P. Rez, E. Soignard, J. Zhu, P. E. Batson, M. J. Lagos, R. F. Egerton,P. A. Crozier, Vibrational spectroscopy in the electron microscope, Nature **514**, 13 (2014).
[32] J. Bernholc, N. O. Lipari, S. T. Pantelides, Self-Consistent Method for Point Defects in Semiconductors: Application to the Vacancy in Silicon, Physical Review Letters **41**, 895-899 (1978).
[33] S. D. Findlay, M. P. Oxley, L. J. Allen, Modeling atomic-resolution scanning transmission electron microscopy images, Microsc Microanal **14**, 48-59 (2008).
[34] H. Kohl, H. Rose, in *Advances in Electronics and Electron Physics*, edited by P. W. Hawkes (Academic Press, 1985), 173-227.
[35] S. J. Pennycook, P. D. Nellist, in *Scanning transmission electron microscopy: imaging and analysis* (Springer Science & Business Media, 2011), **6**, 247-289.
[36] G. Kresse, D. Joubert, From ultrasoft pseudopotentials to the projector augmented-wave method, Physical Review B **59**, 1758-1775 (1999).
[37] G. Kresse, J. Furthmüller, Efficiency of ab-initio total energy calculations for metals and semiconductors using a plane-wave basis set, Computational Materials Science **6**, 15-50 (1996).
[38] G. Kresse, J. Furthmüller, Efficient iterative schemes for \textit{ab initio} total-energy calculations using a plane-wave basis set, Physical Review B **54**, 11169-11186 (1996).
[39] B. Adolph, J. Furthmüller,a. F. Bechstedt, Optical properties of semiconductors using projector-augmented waves, Phys Rev B **63**, 125108 (2001).
[40] K. Hummer, J. Harl, G. Kresse, Heyd-Scuseria-Ernzerhof hybrid functional for calculating the lattice dynamics of semiconductors, Physical Review B **80**, 115205 (2009).
[41] J. Heyd, G. E. Scuseria, M. Ernzerhof, Hybrid functionals based on a screened Coulomb potential, The Journal of Chemical Physics **118**, 8207 (2003).
[42] L. Yang, J. Deslippe, C. H. Park, M. L. Cohen, S. G. Louie, Excitonic effects on the optical response of graphene and bilayer graphene, Phys Rev Lett **103**, 186802 (2009).
[43] C. Hébert, P. Schattschneider, A proposal for dichroic experiments in the electron microscope, Ultramicroscopy **96**, 463-468 (2003).
[44] P. Schattschneider, S. Rubino, C. Hebert, J. Rusz, J. Kunes, P. Novak, E. Carlino, M. Fabrizioli, G. Panaccione, G. Rossi, Detection of magnetic circular dichroism using a transmission electron microscope, Nature **441**, 486-488 (2006).

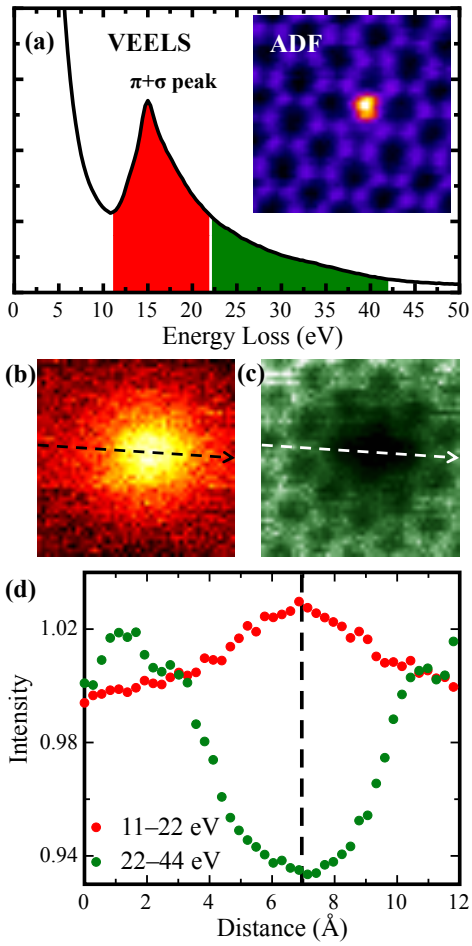

FIG. 1. Experimental STEM/VEELS data of a fourfold-coordinated silicon impurity in graphene. (a) VEELS spectrum showing the position of the π+σ peak at 15 eV. Inset: Annular-dark-field Z-contrast image of a monolayer graphene showing atomic resolution and the position of a fourfold silicon impurity as a bright spot. (b-c) VEELS maps corresponding to integration of the VEEL spectra over the 11-22 eV (red) and 22-44 eV (green) energy ranges as highlighted in (a). (d) Line profiles along the dashed lines in (b) and (c) (average intensities are normalized to 1). **The maps in (b) and (c) are created by the raw spectroscopic data first reported in [28].**

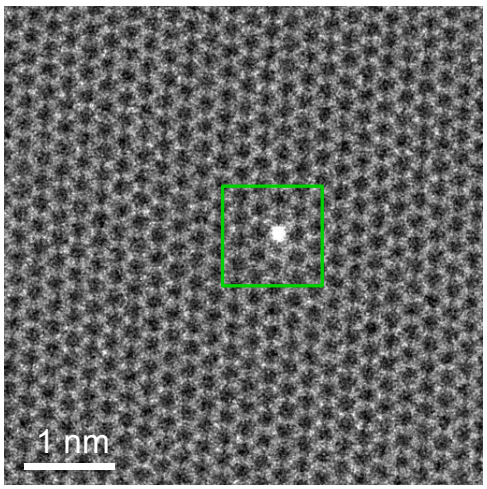

FIG. 2. The fourfold silicon impurity viewed in a lower magnification scale. The green box indicates the area where the VEELS signal of Fig. 1 was acquired.

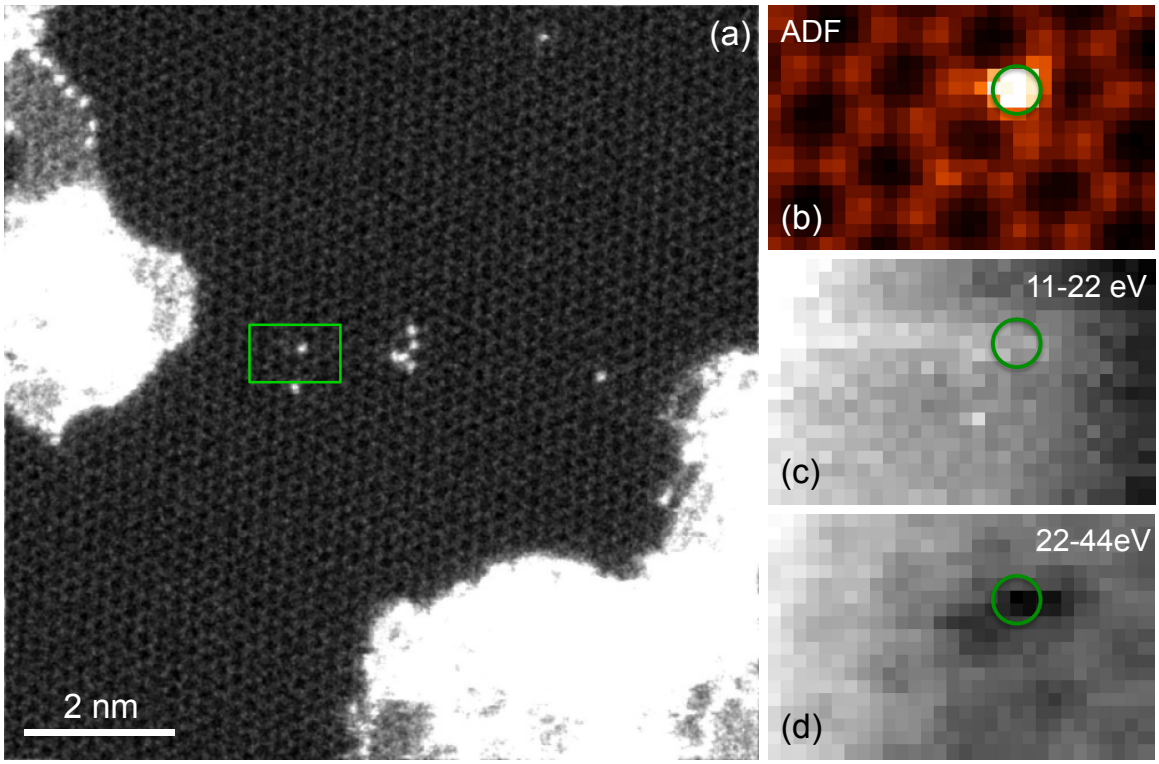

FIG. 3. (a) A lower magnification ADF image of the graphene monolayer showing a threefold coordinated silicon impurity. (b) The ADF image that corresponds to the green box in (a) showing the position of a threefold coordinated silicon impurity. We observe that the 3-fold Si defect is close to other defects, as one can see from the continuously decaying background in the VEELS map of 11-22 eV. However, the enhancement for 11-22 eV and dark contrast for 22-44eV can still be observed at the Si site. The green box in (a) indicates the area where the VEEL signal was acquired. The circles in (b)—(d) indicate the position of the silicon atom.

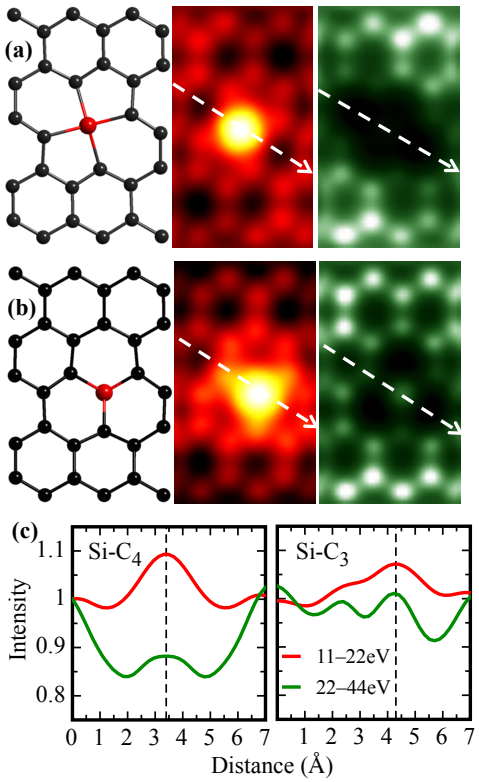

FIG. 4. Simulated STEM/VEELS maps for different bonding configurations of silicon impurities in graphene. (a-b) Left: sketches of the atomic structure matching the area of the maps displayed in the center and right panels; center: calculated VEELS map for E_{LOSS}=11-22 *eV*, right: calculated VEELS map for E_{LOSS}=22-44 eV, corresponding to the experimental maps of Fig. 1(b-c). (c) Line profiles along the dashed lines in the maps in (b) and (c).

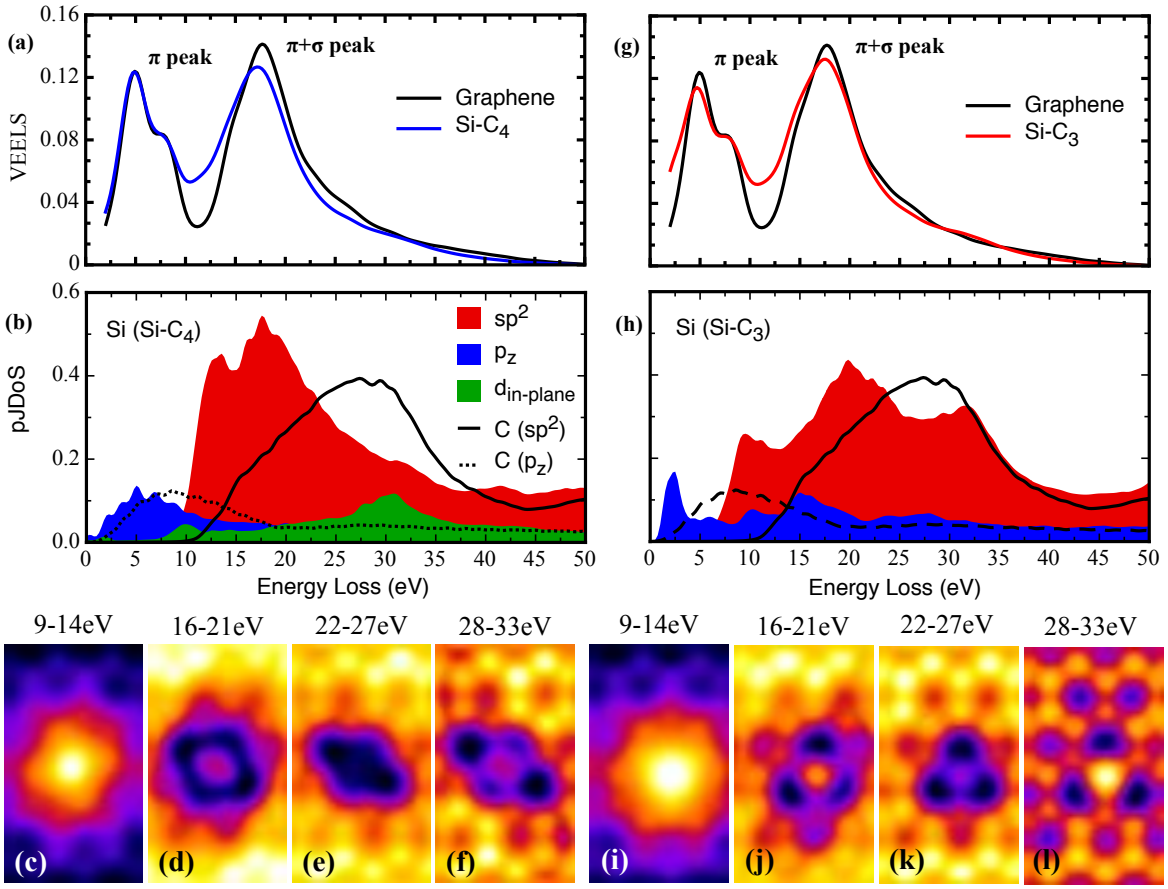

FIG. 5. The origin of the effects of silicon impurities on the VEELS maps and spectra – VEELS maps as impurity signatures (a,g) The calculated VEEL spectra for the fourfold- and threefold-coordinated Si impurity, respectively, compared with the VEEL spectrum of pristine graphene. All VEEL spectra are calculated within an area about 2 $\mathbf{Å^2}$ around the atom of interest. (b, h) The *lm*-decomposed Joint Density of States (PJDOS) projected at the silicon position for the fourfold and threefold-coordinated impurity and at a carbon atom in pristine graphene (black lines). We include only $lm \rightarrow lm$ transitions for illustration purposes (optical selection rules do not apply) (c-f) Calculated VEELS maps within the 9-14 eV (c), 16-21 eV (d), 22-27 eV (e) and 28-33 eV (f) energy ranges for the fourfold-coordinated impurity. (i-l) Calculated VEELS maps for the threefold-coordinated silicon impurity within the same energy windows as in VEELS maps (c-f).

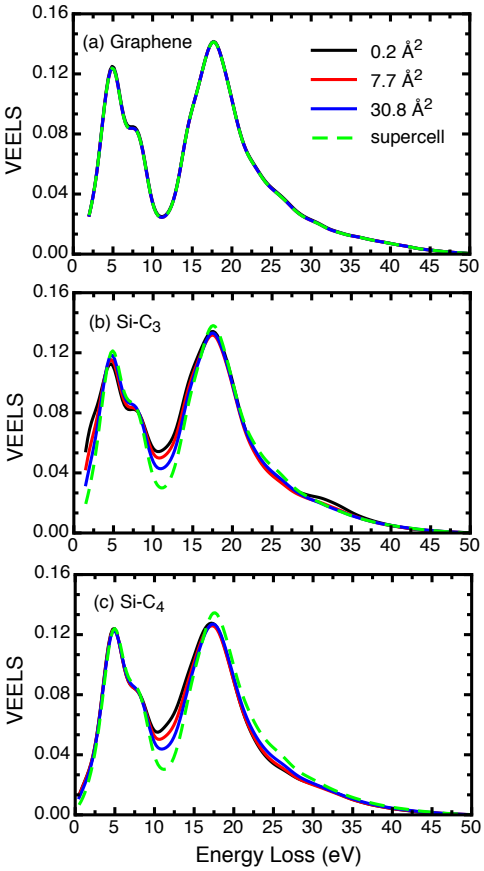

FIG. 6. Calculated VEEL spectra for pristine graphene (a), the system with the threefold- (b) and the fourfold-coordinated (c) silicon impurity for increasing integration area.

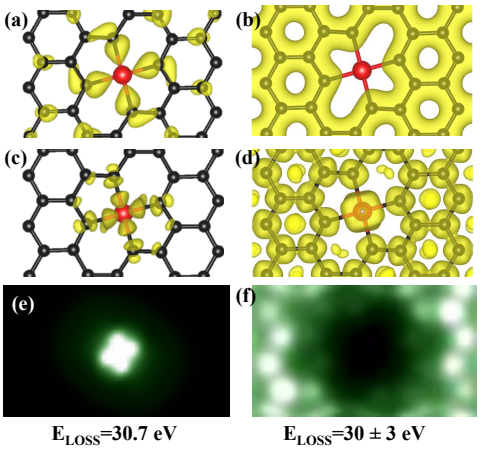

FIG. 7. Characteristic VEELS maps formed by resonant or antiresonant excitations. (a) and (c) Charge densities of two states that are highly localized around the impurity (resonant states). (b) and (d) Charge densities of two states displaying delocalization through the crystal (antiresonant states). (e) VEELS map produced by the pair of resonant states (a) and (c) as initial and final state correspondingly. (f) VEELS maps produced by the antiresonant states (b) and (d) as initial and final state correspondingly. (Charge densities are plotted at the 20% level of isosurfaces).